Research Article Vol. 28, No. 21 / 12 October 2020 / Optics Express 32152

Optics EXPRESS

Optical confinement in the nanocoax: coupling to the fundamental TEM-like mode

YITZI M. CALM,[1] LUKE D'IMPERIO,[1] NATHAN T. NESBITT,[1] JUAN M. MERLO,[1,2] AARON H. ROSE,[1] CHAOBIN YANG,[1] KRZYSZTOF KEMPA,[1] MICHAEL J. BURNS,[1] AND MICHAEL J. NAUGHTON[1,*]

[1]*Boston College Dept. of Physics, 140 Commonwealth Avenue, Chestnut Hill, MA 02467, USA*
[2]*Vassar College Physics and Astronomy Dept., 124 Raymond Avenue, Poughkeepsie, NY 12604, USA*
[*]*naughton@bc.edu*

Abstract: The nanoscale coaxial cable (nanocoax) has demonstrated optical confinement in the visible and the near infrared. We report on a novel nanofabrication process which yields optically addressable, sub-µm diameter, and high aspect ratio metal-insulator-metal nanocoaxes made by atomic layer deposition of Pt and Al_2O_3. We observe sub-diffraction-limited optical transmission *via* the fundamental, TEM-like mode by excitation with a radially polarized optical vortex beam. Our experimental results are based on interrogation with a polarimetric imager. Finite element method numerical simulations support these results, and their uniaxial symmetry was exploited to model taper geometries with both an electrically large volume, $(15\lambda)^3$, and a nanoscopic exit aperture, $(\lambda/200)^2$.

1. Introduction

All multi-conductor waveguides support a TEM-like fundamental mode [1] with no cutoff frequency, and can therefore achieve optical confinement [2] beyond the diffraction limit [3]. Among the common metal-insulator-metal (MIM) topologies, only the coaxial cable [4] totally encloses the insulating space, thus eliminating fringe/stray fields. Theory has predicted [5,6] and early experimental observations [7–10] have demonstrated transmission of visible light (VIS) through sub-µm diameter coaxial MIM structures (*i.e.* nanocoaxes). The nanocoax has numerous optical applications, including color filters [11,12], optical tweezers [13], negative index metamaterials [14], fiber-terminating lenses [15,16], superresolution imaging [17], scanning Raman probes [18], and laser cavities [19,20].

Much of the prior work has excited the nanocoax in dipolar guided modes: predominantly the TE_{11}-like mode, but also in other dipolar modes [21]. Relatively few studies focused specifically on coupling into the fundamental TEM-like (monopolar) mode. One scheme [22–24] involves illuminating with TM-polarized plane waves at oblique angles of incidence, greater than 20°. Another scheme, leveraging the cylindrical symmetry shared by a nanocoax and a Laguerre-Gauss (LG) beam, is to illuminate with a radially polarized optical vortex [24–26]. We follow the latter approach in this work. Most prior experiments [27,28] have studied annular apertures perforating a thin film, so the coaxial MIM structure is a nearly 2D object with length/diameter aspect ratio AR ~ 1. These sub-µm apertures can be readily fabricated by focused ion beam (FIB) milling [29], electron beam lithography [30] (EBL), nanosphere lithography [31], or by photolithography [32].

2. Nanofabrication

Our approach is an extension of atomic layer lithography [33], which exploits the conformal nature of atomic layer deposition (ALD) to determine a structure's transverse dimensions at length scales deeply below the patterning resolution of our lithography systems. Figure 1(a)

#402723 https://doi.org/10.1364/OE.402723
Journal © 2020 Received 16 Jul 2020; revised 11 Sep 2020; accepted 11 Sep 2020; published 9 Oct 2020

Optics EXPRESS

shows the patterning of a nanohole array into a Si substrate *via* EBL and a Bosch deep reactive ion etch (DRIE) [34]. An etched array has three dimensional parameters: hole diameter D, pitch p, and depth L. We repeatably achieve AR = $L/D \sim 20$ and fill factors (FF) of 50%, with D, p, and L typically around 0.5, 0.68, and 10 µm, respectively.

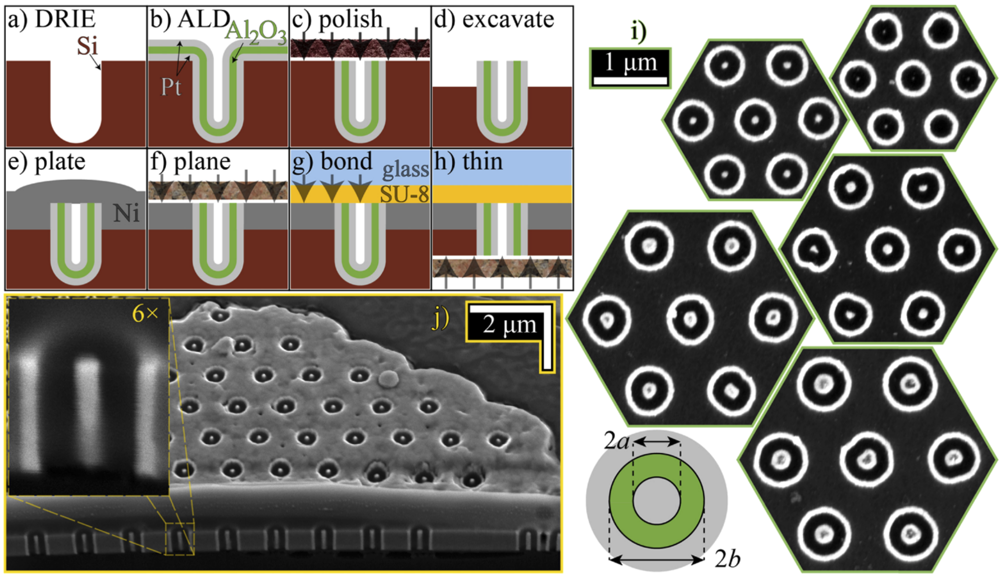

Fig. 1. *Nanofabrication.* (a-h) Schematics for some of the process steps. The resulting structure (h) is a relatively high AR MIM nanocoax which perforates an optically opaque ground plane. Note that atomic layer lithography is readily scaled to much smaller transverse dimensions than those pictured above. (i) After polishing, the coaxial thin films are clearly visible, with coaxial diameters 2a and 2b shown. (j) A FIB cross section of a representative sample, thinned to a final thickness of 0.8 µm.

After DRIE, Fig. 1(b) shows that we conformally coat the MIM layers of the coaxial structure by ALD of Pt and Al_2O_3. Pt is currently the best optical metal with well-established ALD processes [35], noting that processes for Ag and Au films are in development. Further details regarding the ALD steps are discussed after the following paragraph. Figure 1(c) shows how we access these layers by polishing the top side. The cross section of a coaxial waveguide is essentially an insulating annulus with inner and outer diameters 2a and 2b, respectively. The five hexagonal panels of Fig. 1(i) show polished arrays where the constituent film thicknesses $t_{Pt} = 75$ nm and $t_{Al_2O_3} = 150$ nm were deposited into five different hole diameters (D = 400, 450, 500, 550, and 600 nm). As the films are coated radially inward from the sidewalls, the waveguide radii a and b are determined by D and the sum of t_{Pt} and $t_{Al_2O_3}$. The values above result in nanocoaxes which are single mode in the VIS and near infrared (NIR). For sufficiently thick films, the nanohole may clog during the ALD; the final structure has one of the 4 topologies in Table 1.

In Figs. 1(d) and (e) we substitute Ni for Si by "excavating" the Pt/Al_2O_3 nanocoaxes with an isotropic selective etch (CF_4 plasma), and then electroplating several µm of Ni where the Si used to be. The top-side (buried during plating) is re-opened in Fig. 1(f) by mechanical planarization. The nanocoaxes then perforate an optically opaque Ni ground plane, instead of the relatively high transparency crystalline Si. The Ni ground plane is both mechanically refractory and plasmonically inactive. The latter property enables optical addressing of an individual nanocoax by eliminating optical cross talk, and any enhanced/extraordinary optical transmission effects [36]. Figures 1(g) and (h) show, respectively, adhesive bonding [37,38] of the Si substrate to an

Table 1. Nanofabricated waveguide topologies.[a]

range of hole diameters D	resulting topology
$D/2 < t_{Pt}$	wire (metal only)
$t_{Pt} < D/2 < t_{Pt} + t_{Al_2O_3}$	hollow cylindrical (no core)
$t_{Pt} + t_{Al_2O_3} < D/2 < 2t_{Pt} + t_{Al_2O_3}$	coaxial (solid core)
$2t_{Pt} + t_{Al_2O_3} < D/2$	coaxial (hollow core)

[a] Assuming the 1st and 2nd Pt layers have the same thickness, t_{Pt}.

optically transparent glass superstrate using an SU-8 epoxy layer, and then a second mechanical planarization step. The 525 µm thick Si is back-side thinned down to a thickness less than the etched nanohole depth L, thus breaching the back-sides of the nanocoaxes. Figure 1(j) shows a FIB cross sectional image of a finished structure with final thickness 0.8 µm. After flipping the sample, the glass 'superstrate' is relabeled as a 'substrate', with a thin, double-side polished device layer on top.

The optical constants of the ALD Pt and Al_2O_3 films were measured by ellipsometry and are plotted *vs.* free space wavelength λ in Figs. 2(a) and (b), respectively. The Pt films have measured $N = n + i\kappa$ that compare well with reported values [39]. The Al_2O_3 films, with $\kappa \sim 10^{-3}$ typical, are low enough loss relative to metals to be modeled with a lossless Cauchy fit $n = A + B/\lambda^2 + C/\lambda^4$, where $A = 1.6176$, $B = 6{,}400$ nm^2, and $C = 1.3\times10^7$ nm^4. Figures 2(c) and (d) show, respectively, the real parts of the effective mode indices n_{mode} and the propagation lengths plotted *vs.* $2b$.

The curves were computed with a 2D eigenmode solver in COMSOL, considering infinitely long MIM nanocoaxes operating at $\lambda = 980$ nm, with insulator $\mathrm{I} = Al_2O_3$, and fixing $b = 2a$. The 6 curves plotted are for each of the TEM- (blue) and TE_{11}-like (red) modes in coaxes clad by 3 different metals, M = Pt (solid), Ag (dashed) [40], or a perfect electrical conductor (PEC, dot-dashed). We use $n_{Al_2O_3} = 1.624$, $N_{Pt} = 3.4 + 7.1i$, and $N_{Ag} = 0.04 + 7.0i$. Figure 2(c) shows that the TE_{11} mode in the PEC-clad nanocoax cuts off sharply at $2b = 260$ nm, in good agreement with the textbook formula, $\lambda_c^{TE_{11}} \approx \pi n(a + b)$. For Ag-clad nanocoaxes, the cutoff is less sharp and at a smaller $2b = 180$ nm, commensurate with redshifted $\lambda_c^{TE_{11}}$. The redshift in cutoff originates from the mode field diameter increasing with penetration into the lossy metal walls [41]. For Pt-clad nanocoaxes, while the value of $2b$ at cutoff and the propagative n_{mode} are similar to Ag-clad nanocoaxes, Fig. 2(d) shows a clear difference in propagation length. While the high losses of Pt in the VIS and NIR restrict device design to guided propagation distances of *ca.* 1 µm, the conformality of Pt ALD is critical to obtain the coaxial geometry presented in Fig. 1. Figure 2(c) also shows how the guided mode indices asymptotically approach their limiting values, depending on which material in the MIM structure the mode field dominantly overlaps with. Neglecting factors of π, n, and the ratio of b-to-a: for $2b >> \lambda$, $n_{mode} \rightarrow n_{insulator}$; and for $2b << \lambda$, $n_{mode} \rightarrow n_{metal}$. Those limits are obeyed by all lossy-metal guided modes except one: the TEM n_{mode} grows ever larger with decreasing $2b$.

ALD is the linchpin of our approach, so we make a few remarks: First, the coaxial radii a and b are controlled by a digital monolayer process wielding *bona fide* sub-nm dimensional accuracy. Others have achieved extreme optical confinement in this way, squeezing light into gaps less than 5 [42], 2 [43], and even 1 nm [44] wide. Second, we observe conformal Pt deposition for AR > 300, roughly on par with other recent work [45–49]. Third, due to its conformality, ALD can make non-circular (*e.g.* square) concentric MIM waveguides, which still support a totally enclosed, cuffoff-free mode [50].

Optics EXPRESS

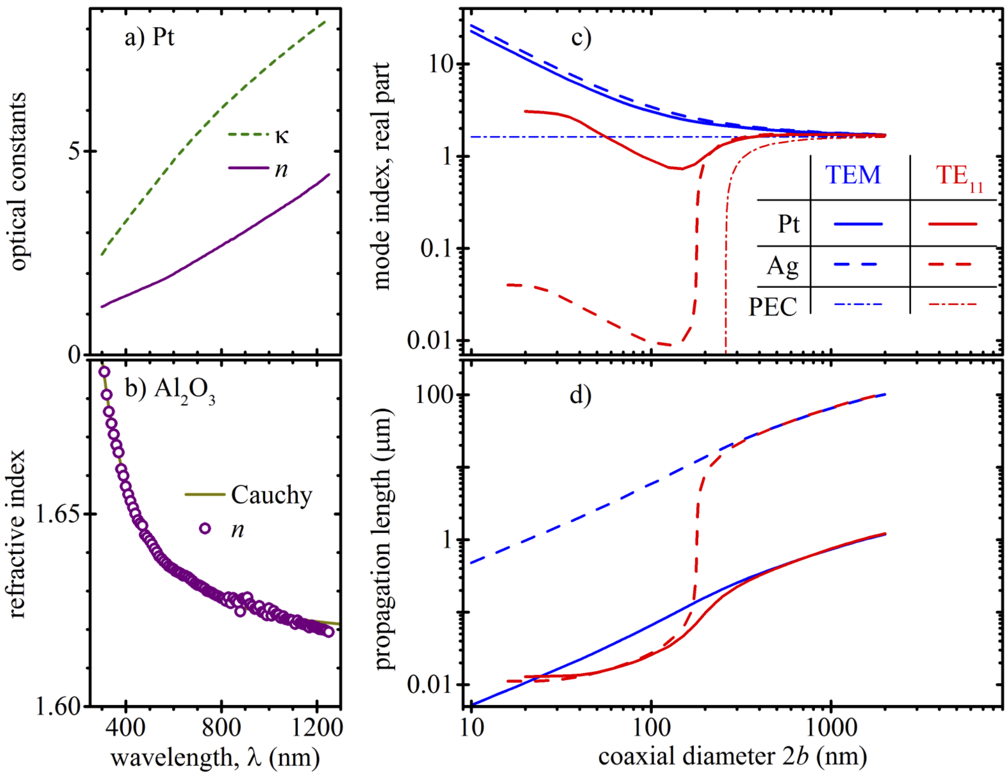

Fig. 2. *Optical Constants and Waveguiding Properties.* (a) Pt optical constants n (solid purple) and κ (dashed green), and (b) Al_2O_3 refractive index n (purple circles) with a Cauchy fit (solid yellow line) plotted *vs.* vacuum wavelength. (c) Mode index and (d) propagation length plotted *vs.* coaxial diameter $2b$ at $\lambda = 980$ nm in an infinitely long $b = 2a$ nanocoax. With an Al_2O_3 insulator, the metal is either Pt (solid lines), Ag (dashed lines), or a PEC (dash-dot lines). Both the TEM (blue) and TE_{11} (red) modes are shown for each metal.

3. Vortex generation and polarimetric imaging

To excite the fundamental, TEM-like mode of the nanocoax [26] we use a 980 nm radially polarized vector beam (*i.e.* a "donut"). A schematic of our optical setup is shown on the left-hand side of Fig. 3. The mirror M3 is flipped in and out of the 980 nm path to use the colinear 670 nm alignment laser. The 980 nm, nominally TEM_{00} beam is conditioned as follows: first, the power is controlled *via* a neutral density filter wheel; second, the beam is expanded then polarized with a director, the $\lambda/2$ waveplate rotates the laser's native (nominally linear) polarization into alignment with the director; third, the beam is spatially filtered and fed to a commercial-off-the-shelf liquid crystal waveplate (Thorlabs Inc.), which converts the linearly polarized Gaussian into a radially polarized donut.

A substrate is positioned with an *xyz*-piezo stage at the common focus shared by coincident inverted and upright microscopes. The inverted microscope focuses the beam at $NA_{beam} = 0.31$ through the transparent substrate's backside. The beam expansion is chosen to optimally fill the inverted microscope objective's back aperture. On the topside, the transmitted light is collected by an upright microscope with either an oil immersion (as pictured) or dry objective at $NA_{obj} = 1.40$ or 0.95, respectively. In the tube space of the upright microscope, we place a rotating analyzer and acquire images with a monochrome CMOS camera at a series of analyzer angles φ, registered absolutely to within 0.1° of the image sensor's x-axis.

Optics EXPRESS

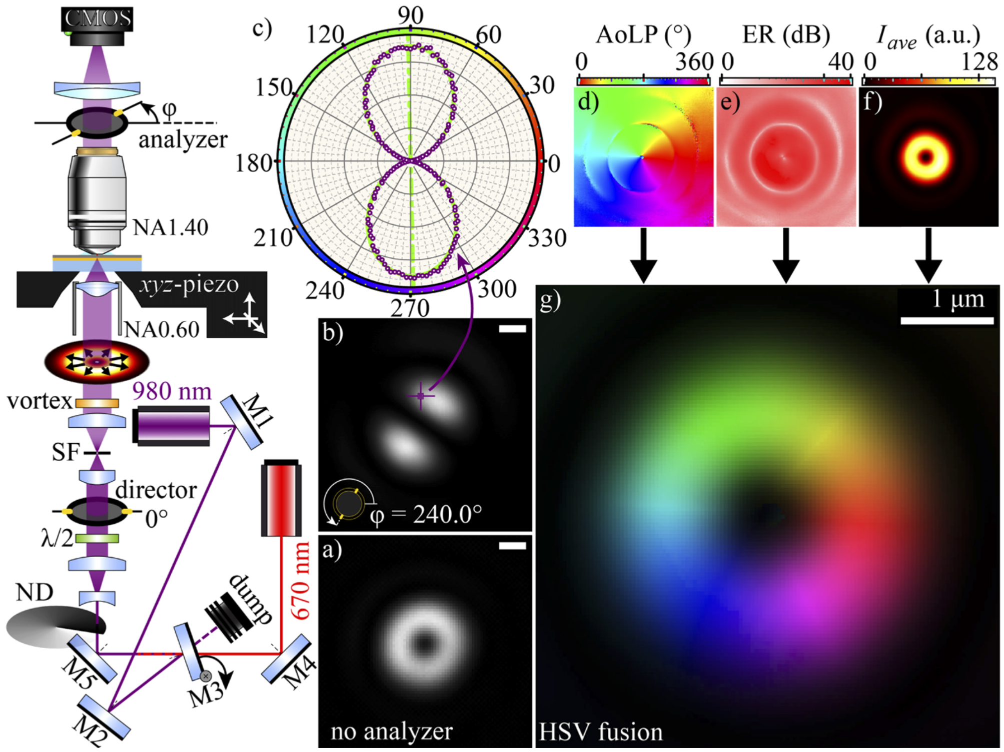

Fig. 3. *Vortex Generation and Polarimetric Imaging.* (left) Optical setup. (a) Donut beam imaged without an analyzer and (b) with an analyzer at $\varphi = 240.0°$. Scale bars: 1 µm. (c) Polarization trace from a pixel outlined with a purple reticle in (b). Three color channels (d-f) are rastered from the pixel-wise polarimetric fits and combined into a 24-bit HSV-fusion image (g). The fusion colors encode the local polarization and intensity of the 980 nm vortex beam.

Figure 3(a) is an image of the donut beam without an analyzer installed, and in Fig. 3(b) one sees how the analyzer picks-off two lobes of the donut with polarization parallel to the analyzer's transmissive axis. The accumulated images form layers of a stack (one layer for each φ). At each pixel in the stack we sample the grayscale intensities with a 5×5 Gaussian kernel and fit to Malus' law

$$I = I_0 + I_1 \cos^2(\varphi - \varphi_0). \tag{1}$$

φ_0 is the angle of linear polarization (AoLP); I_1 and I_0 are the transmitted intensities of linearly polarized and not-linearly-polarized light, respectively.

The polar plot in Fig. 3(c) shows a typical analyzer trace (purple circles) and fit curve (green), with grayscale intensities sampled from the pixels marked with a purple reticle in Fig. 3(b). Those pixels are "due North" (*i.e.* at the polar angle 90°) of the vortex beam's topological singularity, and note how the peak intensity occurs when the analyzer points North or South. The two intensities are equivalently cast in terms of the extinction ratio $\mathrm{ER} = (I_0 + I_1)/I_0$, and the intensity averaged over φ, $I_{ave} = I_0 + I_1/2$. The three parameters AoLP, ER, and I_{ave} are plotted in Figs. 3(d)–(f) by convolving the Gaussian kernel over the image stack. These rasters are combined as channels of the false-colored fusion image shown in Fig. 3(g) by mapping into a cylindrical color space [51,52]. We use the standard formulae for Hue ($\mathrm{H} = \varphi_0$) and Value

(V = I_{ave}). But for Saturation (S), we choose

$$S = \sqrt[3]{10\log_{10}(\mathrm{ER})}. \tag{2}$$

This nonlinear scale helps emphasize [53] the AoLP for pixels with a relatively high ER (*e.g.* the dark pixels with low I_{ave} also generally have a low ER, and we choose to de-emphasize the AoLP at these pixels). In this way, the color saturation is closely connected to the degree of linear polarization. The HSV-fusion image therefore encodes polarization information colorimetrically [54–56]. To the best of our knowledge, this work is the first to apply a full three-channel HSV-fusion method to the polarimetric imaging of a cylindrical vortex beam, although several works [57,58] have used a similar two-channel approach. In concert with the colorimetric scales above, Fig. 3(g) indicates unambiguously our donut beam is radially polarized. Ours is a "division of time, incomplete polarimeter" [59]. We cannot resolve the circular polarization content (some unknown fraction of I_0). However, as Fig. 3(e) shows, with ER > 20 dB typical, this roughly 1% effect can be neglected in these experiments. One direction of future work is to add an indexable waveplate into the microscope tube and capture complete Mueller/Stokes polarimetric images; these complete images, bearing a 4$^{\text{th}}$ piece of polarimetric information, could be color-fused by adding an alpha channel to the above mappings.

4. Far-field transmission via the TEM-like mode

Next we place the nanocoax sample on the microscope stage, and use the piezo nanopositioner to couple the donut beam into guided modes. Shown in Figs. 4(a)–(c) are scanning electron micrographs (SEM's) of nanocoaxes with fixed diameters $2a = 0.4$ μm and $2b = 0.75$ μm, respectively, but with decreasing array pitch p. Figures 4(d)–(f) show the corresponding polarimetric images of those same nanocoaxes transmitting the donut beam. Figure 4(d) shows the principal polarimetric imaging result: a heptamer of nanocoaxes was nanopositioned concentrically with the beam, and the central coax, being centered on the input beam's singularity and sampling only an interior annulus thereof, transmits a smaller radially polarized donut. The peripheral 6 coaxes each transmit linearly polarized "p-orbitals" (*i.e.* with only a single Hue each), and with lobes aligned to the local AoLP. These are direct observations of transmission by the fundamental TEM-like and the first excited TE_{11}-like modes, respectively. For coupling to the TEM-like mode, we note that even though a focused, radially polarized donut is TM-polarized, our $NA_{beam} = 0.31$ focusing subtends angles only up to 12° in the glass substrate, which less than the minimum 20° required for excitation by TM-polarized plane waves [24,60]. The focusing in our setup is too weak to possibly probe that coupling mechanism. So we conclude the coupling is due to direct overlap of the guided mode with the LG beam. Within these experimental conditions, we also find the TE_{11} coupling is the dominant means of transmission for the peripheral 6, much in line with the work of others [7].

Figures 4(a)–(c) show the effect of decreasing pitch p, down to our fabrication limit: when p approaches the its lower limit, $p \rightarrow D$ (*i.e.* etching "kissing cylinders"), the insulating Al_2O_3 layer percolates, so that a continuous layer spans the array.

While the resulting MIM structure no longer an array of disjoint coaxes but rather a periodic coalescence of Pt and Al_2O_3 (at a divided pitch), it is still a multiconductor waveguide and roughly preserves polarization on transmission. Figures 4(d)–(f) show the peripheral p-orbitals merging into the central donut. Figures 4(g)–(i) are SEMs of the densest arrays fabricated, close to the percolation threshold, where the Al_2O_3 annuli subtend about 27% of the area (*i.e.* fill factor, FF ~ 27%). In this sequence, we fix the FF and minify the array, shrinking both the coaxial diameter $2b$ and the pitch p. The transmitted polarimetric images, collected with a dry $NA_{obj} = 0.95$ objective, are shown in Figs. 4(j)–(l), respectively. For the densest array, the transmitted donut (Fig. 4(l)) is indecipherable from the input beam (Fig. 3(g)). Indeed, plotting the fast Fourier transforms (FFT's) of the V-channels in Figs. 4(m)–(o), respectively, one can see

Optics EXPRESS

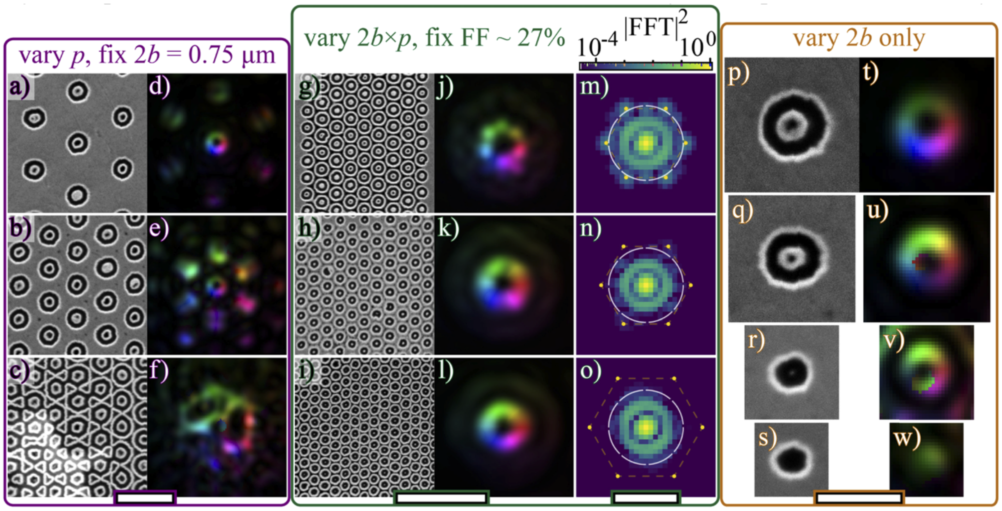

Fig. 4. *Far-field Polarimetry*. (a-f) Coalescence by arrays with fixed coaxial diameter $2b$ and shrinking pitch, p. (g-o) Minimum resolved pitch for fixed FF ~ 27%. FFTs are normalized against their peak. (p-w) Transmission through isolated, individual nanocoaxes, with decreasing diameter $2b$. Scale bars: (a-f) 2 µm, (g-l) 5 µm, (m-o) 10 rad·µm^{-1}, (p-w) 1 µm.

the first order diffracted peaks (highlighted with yellow points at $2\pi/p$ for clarity) stretch further and further outside of the numerical aperture of the upright microscope (white circle) as the array is minified. Therefore, one cannot resolve the pitch of arrays much denser than $p \sim \lambda/\mathrm{NA}$. This means the densely packed coaxes are functioning as a passively phased array: the input beam is sampled discretely on the back side by coupling into the guided modes of many individual nanocoaxes (*e.g.* roughly 50 in Fig. 4(i)), and when emitted on the top side the interference pattern broadcasted by the array resembles an apparently unaffected beam to within the resolving power of the microscope. In our case, the relative phase retardance mapped across the array is near unity, however one could fabricate a non-trivial phase map, for example, by angle-polishing a wedge [14]. By taking the ratio of camera exposure times and normalizing against the FF, we estimate the transmittance of these dense arrays is about 20%; although simulations show that transmittance is strongly wavelength- and thickness-dependent.

Figures 4(p)–(s), show SEM's of individual waveguides fabricated in holes with decreasing diameter D, and Figs. 4(t)–(w) show the corresponding polarimetric images. The transmitted donut size decreases commensurately with size of the coax. This trend is broken for the smallest waveguide which is not a nanocoax (clogged during Al_2O_3 deposition, see Table 1), and does not transmit a donut due to its lack of a central conductor. One should expect strong overlap between a radially polarized donut beam and the TM_{01} mode of a hollow cylindrical waveguide, however for the waveguide shown in Fig. 4(s), one should also expect the TM_{01} mode to cutoff for $\lambda >$ 0.76 µm, which is shorter than our 980 nm source. The expected TE_{11} cutoff for that waveguide is 1.0 µm.

5. Finite element method (FEM) simulation

Our experimental observations are augmented by computational results. We consider two types of LG beams: a radially polarized $|l| = 1$ donut; and a linearly polarized (along $\hat{x}$) $l = 0$ Gaussian, where the integer l gives the azimuthal "twist" in the beam, $\mathbf{E}(\mathbf{r}, t) \propto \exp(il\varphi)$ ($\mathbf{E}$ is the electric field). The most accurate way to model focal fields is by numerically solving diffraction integrals.

A more flexible approach, albeit less accurate, is to use closed-form, approximate expressions. One can ascertain the validity of those expressions by juxtaposing them against the numeric integral results [61]. We use the paraxially approximate formulae:

$$\mathbf{E}_{\hat{x}\text{ - Gaussian}} = E_0 g \left(\hat{x} - i\theta_{beam} \Psi \frac{x}{w} \hat{z} \right), \tag{3}$$

$$\mathbf{E}_{\hat{\rho}\text{ - donut}} = E_0 d \left(\hat{\rho} - i\theta_{beam} \left(\Psi \frac{\rho}{w} - \frac{w_0}{\rho} \right) \hat{z} \right), \tag{4}$$

where,

$$g = \sqrt{\frac{2}{\pi}} \frac{w_0}{w} \exp\left(-\left(\frac{\rho}{w}\right)^2 - i\frac{k\rho^2}{2R} \right) \Psi, \tag{5}$$

$$d = \frac{\sqrt{2}\rho}{w} g\Psi. \tag{6}$$

with the conventional definitions for the beam parameters $\theta_{beam} = w_0/z_0 = 2/kw_0 = \lambda/\pi w_0$, waist w, curvature R, Guoy phase Ψ, and expressed in either Cartesian (x, y, z) or cylindrical (ρ, φ, z) coordinates. Figures 5(a) and (b) plot the energy densities $|\mathbf{E}_{\hat{x}-\text{ Gaussian}}|^2$ and $|\mathbf{E}_{\hat{\rho}-\text{ donut}}|^2$ in the focal plane ($z = 0$), with arrows indicating the transverse components of the electric field (E_x, E_y). Figures 5(c) and (d) show longitudinal ($y = 0$) slices, with contours drawn to span several decades of energy density (98, 50, 10, 1, 0.1, and 0.01% of the peak).

Figures 5(a)–(d) are simply plots of Eqs. (3) and (4) (not FEM results); since there is no closed-form vector beam solution to Maxwell's equations, we make two comments: First, we derived Eqs. (3) and (4) by constructing a paraxially approximate solution to Maxwell's equations [62,63]. This approximation is warranted by the "weak" focusing of the inverted microscope in Fig. 3, where $\sin\theta_{beam} \approx \theta_{beam} = 18.1°$. Equivalent formulae have been derived previously [64,65]. Second, one must consider that the electromagnetic beam is not purely transverse, and must account for the longitudinal components of the fields E_z and H_z [66]. This accounting becomes increasingly necessary as the azimuthal order l and focusing angle θ_{beam} increase [67].

Figure 5(c) shows an unmistakable signature of the finite E_z in Eq. (4): the finite $|\mathbf{E}|$ at the focus $(\rho, \varphi, z) = (0, 0, 0)$ results in all contours below roughly 50% forming a single, connected "butterfly" shape, instead of two separate "cigar" shapes (as would be the case without the $\hat{z}$ term in Eq. (4)).

We use FEM software (COMSOL) to simulate the optical response of a nanocoax illuminated with a focused LG beam. Several recent computational works have studied a focused LG beam with a FEM model [68–70]. We exploit the azimuthal symmetry shared by a nanocoax and an LG beam by working within COMSOL's 2D-axisymmetric formulation. The principal benefit to invoking this symmetry [71] is it allows one to model electrically large bodies of revolution which span volumes that would otherwise be prohibitively large for a Cartesian 3D model. For example, a model size of order $10\times10\times40\ \lambda^3$ solves several times per minute on a desktop computer.

Figures 5(e) and (f) show single, hollow-core, straight Pt/Al_2O_3 nanocoaxes perforating a Ni ground plane and transmitting an LG beam *via* a guided mode, with the x-component of the field E_x plotted in the longitudinal xz-plane. Figure 5(e) shows $\mathbf{E}_{\hat{\rho}-\text{ donut}}$ transmitted *via* the TEM-like mode, and Fig. 5(f) shows $\mathbf{E}_{\hat{x}-\text{ Gaussian}}$ transmitted *via* the TE_{11}-like mode. The transmission preserves the topology l of the input beam. To emphasize the main point of our paper, that a guided mode without cutoff can be *compressed indefinitely,* we change the coaxial geometry from straight to tapered [72–74]. However, as shown in Fig. 2(d), no practical taper geometry can be achieved with Pt due to its material absorption, so instead we simulate Ag-clad tapers. Figures 5(g) and (h) show longitudinal xz-slices of adiabatic Ag/Al_2O_3 coaxial tapers, again plotting E_x. The entrance annular aperture at the bottom of the taper is large enough to

Optics EXPRESS

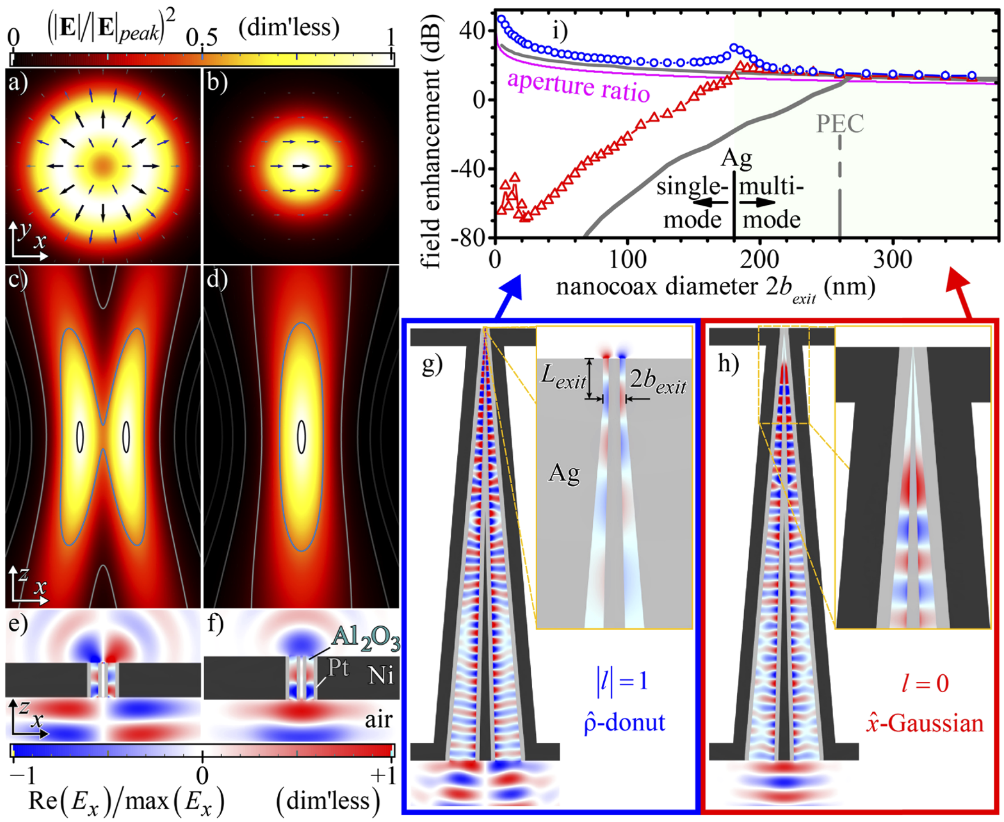

Fig. 5. *Simulation.* (a-d) plots of $|\mathbf{E}|^2$ in vectorial LG beams, Eqs. (3) and (4): (a-b) are cuts in the xz-plane, and (c-d) are cuts in the focal xy-plane. (e-h) FEM results show the computed E_x of LG beams transmitted *via* guided modes through: (e-f) straight Pt/Al_2O_3 nanocoaxes, and (g-h) adiabatically tapered Ag/Al_2O_3 nanocoaxes. (i) Tapered field enhancement *vs.* the coaxial outer diameter $2b_{exit}$ at the exit aperture, with blue circles (red triangles) showing the donut (Gaussian) beam enhancement. The black line at $2b_{exit} = 180$ nm demarcates multi- from single-mode behavior, the gray lines are for a PEC-clad taper, and the magenta curve shows the ratio of exit-to-entrance annular areas.

harvest a significant fraction of the focused LG beam, which couples into a guided mode and gets compressed as it propagates along the taper.

Our mode-matching calculations [75] are given in Table 2, wherein we overlap a focused LG beam with the guided mode of a PEC/Al_2O_3 nanocoax, with coaxial diameters $2a$ and $2b$ representative of both the Pt/Al_2O_3 nanocoaxes we fabricated (as in Fig. 1(j) and Figs. 5(e) and (f)), and of the entrance aperture for the simulated Ag/Al_2O_3 tapers (as in Figs. 5(g) and (h)).

Table 2. Overlapping focused LG beams with PEC/Al_2O_3 nanocoax modes.[a]

	simulated taper entrance $2b/2a = 3.25/1.45$ µm		fabricated $2b/2a = 0.50/0.20$ µm	
	TEM-like	TE_{11}-like	TEM-like	TE_{11}-like
$\mathbf{E}_{\hat{\rho}-\text{ donut}}$	61.4%	< −33 dB	0.5%	< −35 dB
$\mathbf{E}_{\hat{x}-\text{ Gaussian}}$	< −35 dB	18.3%	< −34 dB	5.7%

[a]For a free-space LG beam with $\lambda = 980$ nm and $\theta_{beam} = 18.1°$.

Optics EXPRESS

The off-diagonal terms in Table 2 (*ca.* −34 dB) should be 0 by symmetry; however, as the nanocoax modes are written in terms of the numerical roots to Bessel functions (so the overlap integrals can only be evaluated numerically), these residuals are indicative of the precision to which we computed those integrals. Additional in-coupling efficiency can be gained plasmonically [25,76].

At the top of the taper in Figs. 5(g) and (h), there is a short, straight coaxial section of length L_{exit} which forms a Fabry-Perot-like cavity, bounded below by the impedance gradient in the taper and above by the exit annular aperture. We fix the ratio of the coaxial exit diameters, $b_{exit} = 2a_{exit}$. The insets in Figs. 5(g) and (h) show zoomed views of that termination: the TEM-like mode propagates all the way to the tip (the inset of Fig. 5(g) shows $2b_{exit} = 5$ nm $\approx \lambda/200$); while the TE_{11}-like mode reflects at a point along the taper where the constriction becomes too narrow to support a guided mode at $\lambda = 980$ nm.

To compute the field enhancement plotted in Fig. 5(i), we perform a parametric sweep over the exit aperture coaxial diameter $2b_{exit}$. With the taper length $L_{taper} = 15$ μm fixed, a sweep of $2b_{exit}$ from 300 nm down to 5 nm corresponds to taper angles from 6.2° down to 5.6°. At each value of $2b_{exit}$, we monitor the average field strength at the exit aperture, $\langle|\mathbf{E}_{exit}|\rangle = (b-a)^{-1}\int_a^b dx(|\mathbf{E}(z = L_{taper} + L_{exit})|)$. Keeping the taper geometry fixed, we vary L_{exit}, tuning the exit cavity into resonance and find the maximal value, $\langle|\mathbf{E}_{exit}|\rangle_{max}$. This field strength is then compared to the average field strength $\langle|\mathbf{E}_{entrance}|\rangle$ (using a similar formula as above) of the LG beam focused in air and sampled over an annulus to represent the taper's entrance aperture. We call their ratio, as high as +45 dB, the field enhancement. This corresponds to an intensity enhancement of +90 dB, relative to the focused beam. When $2b_{exit} = 180$ nm in Fig. 5(i), there is a bifurcation between a donut (blue circles) and a Gaussian (red triangles) input, corresponding to the single mode behavior shown in Figs. 2(c) and (d). Note that for single-mode waveguides (with $2b_{exit} < 180$ nm), there are no Fabry-Perot-like resonances and the maximum field enhancement is automatically the shortest tuning length, in order to couple as much of the evanescent TE_{11}-like mode as possible. For the PEC-clad tapers, we find the field enhancement follows roughly the ratio of entrance-to-exit aperture annular areas (plotted with magenta lines).

6. Conclusions

We used conformal ALD to fabricate sub-μm diameter, high AR MIM nanocoaxial waveguides and used a 980 nm radially polarized optical vortex to couple into both the fundamental TEM-like mode and the first excited TE_{11}-like mode. While the coaxes we fabricated are large enough to be multi-mode at $\lambda = 980$ nm, we emphasize that our nanofabrication process is amenable to making much smaller nanocoaxes, for example by choosing different film thicknesses [42]. This is one direction of future work. Another direction is to simulate better-than-linear taper geometries [77,78].

Our work demonstrates a viable pathway towards fabricating and optically addressing nanocoaxial probes for superresolution imaging. The nanocoaxes we fabricated pick off only an interior annulus of the focused donut beam, and therefore transmit a significantly smaller donut. Our simulations of adiabatically tapered nanocoaxial waveguides elucidate an intuitively understood phenomenon: that a cutoff-free guided mode can be confined to *arbitrarily smaller* length scales than the free space wavelength. Our simulations also show a diverging field enhancement as the exit aperture coax is minified below $2b_{exit} < 40$ nm; suggesting these structures' potential use in enhanced light-matter interaction applications.

Optics EXPRESS

Acknowledgements

We acknowledge Steve Shepard at the Boston College Integrated Sciences Cleanroom and Nanofabrication Facility, Rich Pijar and Paul Dee at Boston College's Scientific Instrumentation and Machining Services.

Disclosures

The authors declare no conflicts of interest.

References

1. D. M. Pozar, *Microwave Engineering*, 4th ed. (John Wiley & Sons, Inc., 2012).
2. A. Mahigir, P. Dastmalchi, G. Veronis, W. Shin, P. B. Catrysse, M. L. Brongersma, S. Fan, and W. Cai, "Subwavelength Plasmonic Two-Conductor Waveguides," in *Wiley Encyclopedia of Electrical and Electronics Engineering* (John Wiley & Sons, Inc., 2016), (7), pp. 1–15.
3. Y. M. Calm, J. M. Merlo, M. J. Burns, and M. J. Naughton, "From Airy to Abbe: quantifying the effects of wide-angle focusing for scalar spherical waves," J. Opt. **19**(10), 105608 (2017).
4. W. Thomson, "LXXIV. On the electro-statical capacity of a Leyden phial and of a telegraph wire insulated in the axis of a cylindrical conducting sheath," London, Edinburgh, Dublin Philos. Mag. J. Sci. **9**(62), 531–535 (1855).
5. A. J. Ward and J. B. Pendry, "The theory of SNOM: A novel approach," J. Mod. Opt. **44**(9), 1703–1714 (1997).
6. F. I. Baida and D. Van Labeke, "Light transmission by subwavelength annular aperture arrays in metallic films," Opt. Commun. **209**(1-3), 17–22 (2002).
7. W. Fan, S. Zhang, B. Minhas, K. J. Malloy, and S. R. J. Brueck, "Enhanced Infrared Transmission through Subwavelength Coaxial Metallic Arrays," Phys. Rev. Lett. **94**(3), 033902 (2005).
8. J. Salvi, M. Roussey, F. I. Baida, M.-P. Bernal, A. Mussot, T. Sylvestre, H. Maillotte, D. Van Labeke, A. Perentes, I. Utke, C. Sandu, P. Hoffmann, and B. Dwir, "Annular aperture arrays: study in the visible region of the electromagnetic spectrum," Opt. Lett. **30**(13), 1611 (2005).
9. S. M. Orbons, D. Freeman, B. Luther-Davies, B. C. Gibson, S. T. Huntington, D. N. Jamieson, and A. Roberts, "Optical properties of silver composite metamaterials," Phys. B (Amsterdam, Neth.) **394**(2), 176–179 (2007).
10. J. Rybczynski, K. Kempa, A. Herczynski, Y. Wang, M. J. Naughton, Z. F. Ren, Z. P. Huang, D. Cai, and M. Giersig, "Subwavelength waveguide for visible light," Appl. Phys. Lett. **90**(2), 021104 (2007).
11. G. Si, Y. Zhao, H. Liu, S. Teo, M. Zhang, T. Jun Huang, A. J. Danner, and J. Teng, "Annular aperture array based color filter," Appl. Phys. Lett. **99**(3), 033105 (2011).
12. R. Rajasekharan Unnithan, M. Sun, X. He, E. Balaur, A. Minovich, D. Neshev, E. Skafidas, and A. Roberts, "Plasmonic Colour Filters Based on Coaxial Holes in Aluminium," Materials **10**(4), 383 (2017).
13. A. A. E. Saleh and J. A. Dionne, "Toward Efficient Optical Trapping of Sub-10-nm Particles with Coaxial Plasmonic Apertures," Nano Lett. **12**(11), 5581–5586 (2012).
14. S. P. Burgos, R. de Waele, A. Polman, and H. A. Atwater, "A single-layer wide-angle negative-index metamaterial at visible frequencies," Nat. Mater. **9**(5), 407–412 (2010).
15. Y. Liu, H. Xu, F. Stief, N. Zhitenev, and M. Yu, "Far-field superfocusing with an optical fiber based surface plasmonic lens made of nanoscale concentric annular slits," Opt. Express **19**(21), 20233 (2011).
16. M. Pu, X. Ma, Z. Zhao, X. Li, Y. Wang, H. Gao, C. Hu, P. Gao, C. Wang, and X. Luo, "Near-field collimation of light carrying orbital angular momentum with bull's-eye-assisted plasmonic coaxial waveguides," Sci. Rep. **5**(1), 12108 (2015).
17. K. Kempa, X. Wang, Z. F. Ren, and M. J. Naughton, "Discretely guided electromagnetic effective medium," Appl. Phys. Lett. **92**(4), 043114 (2008).
18. A. Weber-Bargioni, A. Schwartzberg, M. Cornaglia, A. Ismach, J. J. Urban, Y. Pang, R. Gordon, J. Bokor, M. B. Salmeron, D. F. Ogletree, P. Ashby, S. Cabrini, and P. J. Schuck, "Hyperspectral Nanoscale Imaging on Dielectric Substrates with Coaxial Optical Antenna Scan Probes," Nano Lett. **11**(3), 1201–1207 (2011).
19. M. Khajavikhan, A. Simic, M. Katz, J. H. Lee, B. Slutsky, A. Mizrahi, V. Lomakin, and Y. Fainman, "Thresholdless nanoscale coaxial lasers," Nature **482**(7384), 204–207 (2012).
20. A. A. E. Saleh and J. A. Dionne, "Waveguides with a silver lining: Low threshold gain and giant modal gain in active cylindrical and coaxial plasmonic devices," Phys. Rev. B **85**(4), 045407 (2012).
21. J. M. Merlo, F. Ye, B. Rizal, M. J. Burns, and M. J. Naughton, "Near-field observation of light propagation in nanocoax waveguides," Opt. Express **22**(12), 14148 (2014).
22. F. I. Baida, A. Belkhir, O. Arar, E. H. Barakat, J. Dahdah, C. Chemrouk, D. Van Labeke, C. Diebold, N. Perry, and M.-P. Bernal, "Enhanced optical transmission by light coaxing: Mechanism of the TEM-mode excitation," Micron **41**(7), 742–745 (2010).
23. A. Ndao, J. Salvi, R. Salut, M.-P. Bernal, T. Alaridhee, A. Belkhir, and F. I. Baida, "Resonant optical transmission through sub-wavelength annular apertures caused by a plasmonic transverse electromagnetic (TEM) mode," J. Opt. **16**(12), 125009 (2014).
24. A. Roberts, "Beam transmission through hole arrays," Opt. Express **18**(3), 2528 (2010).

25. G. M. Lerman, A. Yanai, and U. Levy, "Demonstration of Nanofocusing by the use of Plasmonic Lens Illuminated with Radially Polarized Light," Nano Lett. **9**(5), 2139–2143 (2009).
26. P. Banzer, J. Kindler, S. Quabis, U. Peschel, and G. Leuchs, "Extraordinary transmission through a single coaxial aperture in a thin metal film," Opt. Express **18**(10), 10896 (2010).
27. Y. Poujet, J. Salvi, and F. I. Baida, "90% Extraordinary optical transmission in the visible range through annular aperture metallic arrays," Opt. Lett. **32**(20), 2942 (2007).
28. R. de Waele, S. P. Burgos, A. Polman, and H. A. Atwater, "Plasmon Dispersion in Coaxial Waveguides from Single-Cavity Optical Transmission Measurements," Nano Lett. **9**(8), 2832–2837 (2009).
29. M. Melli, A. Polyakov, D. Gargas, C. Huynh, L. Scipioni, W. Bao, D. F. Ogletree, P. J. Schuck, S. Cabrini, and A. Weber-Bargioni, "Reaching the Theoretical Resonance Quality Factor Limit in Coaxial Plasmonic Nanoresonators Fabricated by Helium Ion Lithography," Nano Lett. **13**(6), 2687–2691 (2013).
30. M. A. van de Haar and A. Polman, "Fabrication process of a coaxial plasmonic metamaterial," Opt. Mater. Express **6**(3), 884 (2016).
31. H. Ni, M. Wang, T. Shen, and J. Zhou, "Self-Assembled Large-Area Annular Cavity Arrays with Tunable Cylindrical Surface Plasmons for Sensing," ACS Nano **9**(2), 1913–1925 (2015).
32. W. Fan, S. Zhang, K. J. J. Malloy, and S. R. J. R. J. Brueck, "Enhanced mid-infrared transmission through nanoscale metallic coaxial-aperture arrays," Opt. Express **13**(12), 4406–4413 (2005).
33. X. Chen, H.-R. Park, M. Pelton, X. Piao, N. C. Lindquist, H. Im, Y. J. Kim, J. S. Ahn, K. J. Ahn, N. Park, D.-S. Kim, and S.-H. Oh, "Atomic layer lithography of wafer-scale nanogap arrays for extreme confinement of electromagnetic waves," Nat. Commun. **4**(1), 2361 (2013).
34. L. A. Woldering, R. Willem Tjerkstra, H. V. Jansen, I. D. Setija, and W. L. Vos, "Periodic arrays of deep nanopores made in silicon with reactive ion etching and deep UV lithography," Nanotechnology **19**(14), 145304 (2008).
35. S. Barry, *Group 11 Thin Films by Atomic Layer Deposition* (2018), **13**(2).
36. S. M. Orbons, M. I. Haftel, C. Schlockermann, D. Freeman, M. Milicevic, T. J. Davis, B. Luther-Davies, D. N. Jamieson, and A. Roberts, "Dual resonance mechanisms facilitating enhanced optical transmission in coaxial waveguide arrays," Opt. Lett. **33**(8), 821 (2008).
37. F. Niklaus, G. Stemme, J. Q. Lu, and R. J. Gutmann, "Adhesive wafer bonding," J. Appl. Phys. **99**(3), 031101 (2006).
38. R. S. Lima, P. A. G. C. Leão, M. H. O. Piazzetta, A. M. Monteiro, L. Y. Shiroma, A. L. Gobbi, and E. Carrilho, "Sacrificial adhesive bonding: a powerful method for fabrication of glass microchips," Sci. Rep. **5**(1), 13276 (2015).
39. A. D. Rakić, A. B. Djurišić, J. M. Elazar, and M. L. Majewski, "Optical properties of metallic films for vertical-cavity optoelectronic devices," Appl. Opt. **37**(22), 5271 (1998).
40. P. B. Johnson and R. W. Christy, "Optical Constants of the Noble Metals," Phys. Rev. B **6**(12), 4370–4379 (1972).
41. F. I. I. Baida, A. Belkhir, D. Van Labeke, and O. Lamrous, "Subwavelength metallic coaxial waveguides in the optical range: Role of the plasmonic modes," Phys. Rev. B **74**(20), 205419 (2006).
42. D. Yoo, N.-C. Nguyen, L. Martin-Moreno, D. A. Mohr, S. Carretero-Palacios, J. Shaver, J. Peraire, T. W. Ebbesen, and S.-H. Oh, "High-Throughput Fabrication of Resonant Metamaterials with Ultrasmall Coaxial Apertures via Atomic Layer Lithography," Nano Lett. **16**(3), 2040–2046 (2016).
43. H.-R. Park, S. Namgung, X. Chen, N. C. Lindquist, V. Giannini, Y. Francescato, S. A. Maier, and S.-H. Oh, "Perfect Extinction of Terahertz Waves in Monolayer Graphene over 2-nm-Wide Metallic Apertures," Adv. Opt. Mater. **3**(5), 667–673 (2015).
44. D. Yoo, F. Vidal-Codina, C. Ciracì, N. Nguyen, D. R. Smith, J. Peraire, and S. Oh, "Modeling and observation of mid-infrared nonlocality in effective epsilon-near-zero ultranarrow coaxial apertures," Nat. Commun. **10**(1), 4476 (2019).
45. L. K. Tan, A. S. M. Chong, X. S. E. Tang, and H. Gao, "Combining Atomic Layer Deposition with a Template-Assisted Approach To Fabricate Size-Reduced Nanowire Arrays on Substrates and Their Electrochemical Characterization," J. Phys. Chem. C **111**(13), 4964–4968 (2007).
46. P. Banerjee, I. Perez, L. Henn-Lecordier, S. B. Lee, and G. W. Rubloff, "Nanotubular metal–insulator–metal capacitor arrays for energy storage," Nat. Nanotechnol. **4**(5), 292–296 (2009).
47. G. Pardon, H. K. Gatty, G. Stemme, W. Van Der Wijngaart, and N. Roxhed, "Pt–Al2O3 dual layer atomic layer deposition coating in high aspect ratio nanopores," Nanotechnology **24**(1), 015602 (2013).
48. A. Vaish, S. Krueger, M. Dimitriou, C. Majkrzak, D. J. Vanderah, L. Chen, and K. Gawrisch, "Enhancing the platinum atomic layer deposition infiltration depth inside anodic alumina nanoporous membrane," J. Vac. Sci. Technol., A **33**(1), 01A148 (2015).
49. R. He, P. J. A. Sazio, A. C. Peacock, N. Healy, J. R. Sparks, M. Krishnamurthi, V. Gopalan, and J. V. Badding, "Integration of gigahertz-bandwidth semiconductor devices inside microstructured optical fibres," Nat. Photonics **6**(3), 174–179 (2012).
50. W. Shin, W. Cai, P. B. Catrysse, G. Veronis, M. L. Brongersma, and S. Fan, "Broadband Sharp 90-degree Bends and T-Splitters in Plasmonic Coaxial Waveguides," Nano Lett. **13**(10), 4753–4758 (2013).
51. J. S. Tyo, E. N. Pugh, and N. Engheta, "Colorimetric representations for use with polarization-difference imaging of objects in scattering media," J. Opt. Soc. Am. A **15**(2), 367 (1998).
52. A. W. Kruse, A. S. Alenin, and J. S. Tyo, "Review of visualization methods for passive polarization imaging," Opt. Eng. **58**(08), 1 (2019).

53. J. Scott Tyo, B. M. Ratliff, and A. S. Alenin, "Adapting the HSV polarization-color mapping for regions with low irradiance and high polarization," Opt. Lett. **41**(20), 4759 (2016).
54. J. Craven-Jones, M. W. Kudenov, M. G. Stapelbroek, and E. L. Dereniak, "Infrared hyperspectral imaging polarimeter using birefringent prisms," Appl. Opt. **50**(8), 1170 (2011).
55. M. Axer, K. Amunts, D. Grässel, C. Palm, J. Dammers, H. Axer, U. Pietrzyk, and K. Zilles, "A novel approach to the human connectome: Ultra-high resolution mapping of fiber tracts in the brain," NeuroImage **54**(2), 1091–1101 (2011).
56. S. Aïnouz, J. Zallat, A. de Martino, and C. Collet, "Physical interpretation of polarization-encoded images by color preview," Opt. Express **14**(13), 5916 (2006).
57. E. J. Galvez, B. L. Rojec, V. Kumar, and N. K. Viswanathan, "Generation of isolated asymmetric umbilics in light's polarization," Phys. Rev. A **89**(3), 031801 (2014).
58. B. Khajavi and E. J. Galvez, "Preparation of Poincaré beams with a same-path polarization/spatial-mode interferometer," Opt. Eng. **54**(11), 111305 (2015).
59. R. A. Chipman, "Polarimetry," in *Handbook of Optics*, Vol. 1, M. Bass, ed., 3rd ed. (McGraw-Hill, 2010), pp. 15.1–46.
60. A. Ndao, A. Belkhir, R. Salut, and F. I. Baida, "Slanted annular aperture arrays as enhanced-transmission metamaterials: Excitation of the plasmonic transverse electromagnetic guided mode," Appl. Phys. Lett. **103**(21), 211901 (2013).
61. J. Peatross, M. Berrondo, D. Smith, and M. Ware, "Vector fields in a tight laser focus: comparison of models," Opt. Express **25**(13), 13990 (2017).
62. W. L. Erikson and S. Singh, "Polarization properties of Maxwell-Gaussian laser beams," Phys. Rev. E **49**(6), 5778–5786 (1994).
63. W. E. Lewis and R. Vyas, "Maxwell-Gaussian beams with cylindrical polarization," J. Opt. Soc. Am. A **31**(7), 1595 (2014).
64. H. A. Haus, *Waves and Fields in Optoelectronics* (Prentice Hall, 1985).
65. L. W. Davis and G. Patsakos, "TM and TE electromagnetic beams in free space," Opt. Lett. **6**(1), 22 (1981).
66. A. Carnicer, I. Juvells, D. Maluenda, R. Martínez-Herrero, and P. M. Mejías, "On the longitudinal component of paraxial fields," Eur. J. Phys. **33**(5), 1235–1247 (2012).
67. V. Shvedov and W. Krolikowski, "Instantaneous field singularities in electromagnetic waves," New J. Phys. **20**(10), 103034 (2018).
68. K. Sakai, K. Nomura, T. Yamamoto, and K. Sasaki, "Excitation of Multipole Plasmons by Optical Vortex Beams," Sci. Rep. **5**(1), 8431 (2015).
69. W. Shang, F. Xiao, W. Zhu, L. Han, T. Mei, and J. Zhao, "Characterizing localized surface plasmon resonances using focused radially polarized beam," Appl. Opt. **58**(21), 5812 (2019).
70. W. Chen and Q. Zhan, "Numerical study of an apertureless near field scanning optical microscope probe under radial polarization illumination," Opt. Express **15**(7), 4106 (2007).
71. F. I. Baida, D. Van Labeke, and B. Guizal, "Enhanced confined light transmission by single subwavelength apertures in metallic films," Appl. Opt. **42**(34), 6811 (2003).
72. H. Choo, M.-K. Kim, M. Staffaroni, T. J. Seok, J. Bokor, S. Cabrini, P. J. Schuck, M. C. Wu, and E. Yablonovitch, "Nanofocusing in a metal–insulator–metal gap plasmon waveguide with a three-dimensional linear taper," Nat. Photonics **6**(12), 838–844 (2012).
73. M. Schnell, P. Alonso-González, L. Arzubiaga, F. Casanova, L. E. Hueso, A. Chuvilin, and R. Hillenbrand, "Nanofocusing of mid-infrared energy with tapered transmission lines," Nat. Photonics **5**(5), 283–287 (2011).
74. J. Xu, K. Li, S. Zhang, X. Lu, N. Shi, Z. Tan, Y. Lu, N. Liu, B. Zhang, and Z. Liang, "Field-enhanced nanofocusing of radially polarized light by a tapered hybrid plasmonic waveguide with periodic grooves," Appl. Opt. **58**(3), 588 (2019).
75. J. Kindler, P. Banzer, S. Quabis, U. Peschel, and G. Leuchs, "Waveguide properties of single subwavelength holes demonstrated with radially and azimuthally polarized light," Appl. Phys. B **89**(4), 517–520 (2007).
76. A. A. E. Saleh, S. Sheikhoelislami, S. Gastelum, and J. A. Dionne, "Grating-flanked plasmonic coaxial apertures for efficient fiber optical tweezers," Opt. Express **24**(18), 20593 (2016).
77. R. Klopfenstein, "A Transmission Line Taper of Improved Design," Proc. IRE **44**(1), 31–35 (1956).
78. A. Rusina, M. Durach, K. A. Nelson, and M. I. Stockman, "Nanoconcentration of terahertz radiation in plasmonic waveguides," Opt. Express **16**(23), 18576 (2008).